HHS Public Access

Author manuscript

Adv Funct Mater. Author manuscript; available in PMC 2023 November 29.

Published in final edited form as:

Adv Funct Mater. 2021 June 23; 31(26): . doi:10.1002/adfm.202100915.

Broadband Forward Light Scattering by Architectural Design of Core–Shell Silicon Particles

Maria Letizia De Marco,
CNRS, Univ. Bordeaux, Bordeaux INP, ICMCB, UMR 5026, Pessac F-33600, France

Taizhi Jiang,
McKetta Department of Chemical Engineering, 200 E Dean Keeton St, The University of Texas at Austin, Austin TX 78712, USA

Jie Fang,
Walker Department of Mechanical Engineering and Texas Materials Institute, 204 E Dean Keeton St, The University of Texas at Austin, Austin TX 78712, USA

Sabrina Lacomme,
Univ. Bordeaux, CNRS, INSERM, Bordeaux Imaging Center, BIC, UMS 3420, US 4, Bordeaux F-33000, France

Yuebing Zheng,
Walker Department of Mechanical Engineering and Texas Materials Institute, 204 E Dean Keeton St, The University of Texas at Austin, Austin TX 78712, USA

Alexandre Baron,
CNRS, Univ. Bordeaux, CRPP, UMR 5031, Pessac F-33600, France

Brian A. Korgel,
McKetta Department of Chemical Engineering, 200 E Dean Keeton St, The University of Texas at Austin, Austin TX 78712, USA

Philippe Barois,
CNRS, Univ. Bordeaux, CRPP, UMR 5031, Pessac F-33600, France

Glenna L. Drisko,
CNRS, Univ. Bordeaux, Bordeaux INP, ICMCB, UMR 5026, Pessac F-33600, France

Cyril Aymonier
CNRS, Univ. Bordeaux, Bordeaux INP, ICMCB, UMR 5026, Pessac F-33600, France

Abstract

A goal in the field of nanoscale optics is the fabrication of nanostructures with strong directional light scattering at visible frequencies. Here, the synthesis of Mie-resonant core–shell particles with

glenna.drisko@icmcb.cnrs.fr; cyril.aymonier@icmcb.cnrs.fr; philippe.barois@crpp.cnrs.fr.

Conflict of Interest
The authors declare no conflict of interest.

Supporting Information
Supporting Information is available from the Wiley Online Library or from the author.

overlapping electric and magnetic dipole resonances in the visible spectrum is demonstrated. The core consists of silicon surrounded by a lower index silicon oxynitride (SiO_xN_y) shell of an adjustable thickness. Optical spectroscopies coupled to Mie theory calculations give the first experimental evidence that the relative position and intensity of the magnetic and electric dipole resonances are tuned by changing the core–shell architecture. Specifically, coating a high-index particle with a low-index shell coalesces the dipoles, while maintaining a high scattering efficiency, thus generating broadband forward scattering. This synthetic strategy opens a route toward metamaterial fabrication with unprecedented control over visible light manipulation.

Keywords

core–shell particles; directional light scattering; Huygens sources; visible light silicon resonators

1. Introduction

In conventional optics at visible-light frequencies, optical properties result solely from the electric polarization of matter.[1] Metamaterials have emerged as a new class of materials designed to provide a companion magnetic polarization, whereby unparalleled light steering is anticipated.[2] Commanding both electric and magnetic response to light opens the way to extraordinary properties such as cloaking,[3,4] negative refraction and perfect lensing,[2,5] and broadband total transmission or reflection,[6–8] to name a few. The realization of metamaterials requires the design of resonant units (e.g., particles) exhibiting a strong magnetic response, ideally with a magnetic scattering efficiency larger than one, and of subwavelength size to preserve optical homogeneity.[9]

High refractive index dielectric particles are appealing as they naturally sustain intense magnetic and electric Mie resonances, with low light absorption,[10–12] which is the limiting factor for plasmonic nanoparticles.[13] Crystalline silicon presents the best optimization of refractive index and absorption coefficient in the visible among currently known materials.[14] However, spherical silicon particles exhibit well separated dipolar resonances, which results in wavelength dependent angular scattering, precluding their applications as Huygens sources. Merging the two dipolar resonances is of considerable interest to enable high efficiency broadband forward scattering.[15] The electric and magnetic Mie resonances can be overlapped by reducing the refractive index,[16] employing clusters of particles,[17] introducing shape anisotropy[6,15] or designing a core–shell architecture.[18,19] Spherical core–shell particles are insensitive to the direction and polarization of the incident light and thus have advantages over anisotropic particles. Naraghi et al. theoretically proposed the first core–shell particle design composed of two dielectrics with different refractive indexes displaying either total forward scattering or near zero forward scattering by adjusting the core-to-shell radii ratio.[20] Tsuchimoto et al. demonstrated core–shell $Si@SiO_2$ particles with a forward-to-backward scattering ratio five times higher than the bare Si particle, thanks to the coating SiO_2 shell.[19] However, to date, no report exists for the bottom-up synthesis of silicon-based core–shell resonators active in the visible range.

Here, we demonstrate a colloidal synthesis involving the decomposition of bis(*N*,*N*′-diisopropylbutylamidinato)dichlorosilane (silicon bisamidinate, a custom designed silicon coordination compound) with trisilane in supercritical n-hexane (P_c = 30.3 bar and T_c = 235 °C) to generate highly uniform core–shell Si nanoparticles with tunable optical electric and magnetic dipole resonances in the visible spectrum. The core size and shell thickness can be adjusted by simply changing the molar ratio between the two silane precursors. Measurements and simulations of the scattering properties show that these silicon-based core–shell particles exhibit strong magnetic scattering at visible frequencies and that the electric and magnetic dipolar resonances can be superimposed by tuning the core-to-shell ratio, thus validating the concept of a high index core encapsulated in a lower index shell to obtain total forward scattering.[19]

2. Experimental Approach to Produce Silicon Core–Shell Particles

Supercritical fluid-based synthesis is among the most promising bottom-up methods for silicon fabrication.[21–23] The decomposition of trisilane in supercritical n-hexane yields monodisperse, submicron spherical particles of hydrogenated silicon. These particles exhibit well separated electric and magnetic dipole scattering in the near infrared spectrum.[22] Previously reported diameters range between 400 and 1000 nm.[21] Here, silicon particle size is reduced and a core–shell architecture is obtained by mixing trisilane with silicon bisamidinate in supercritical *n*-hexane (Figure 1A). Three different Si bisamidinate to trisilane molar ratios are investigated: 1/5, 1/20, and 1/40. Particles obtained from pure trisilane provide a control sample to assess the role of the Si bisamidinate coordination compound on the size, architecture, and optical properties of the particles.

Spherical, monodisperse particles are obtained with variable core and shell dimensions that depend on the ratio of the two precursors (Figure 1B–J; Figure S3 and Table S3, Supporting Information). Particles made from only trisilane have a 10 nm diffuse layer with a significant amount of oxygen, whereas particles made from the two precursors have a core–shell architecture with a well-defined edge between a silicon core and a shell (Figure 1B–I) containing silicon, oxygen, and nitrogen (SiO_xN_y). The incorporated nitrogen originates from the thermal decomposition of the Si bisamidinate complex (Figure S4, Supporting Information). The nitrogen-containing shell is most likely more porous, and thus prone to oxidation upon particle exposure to the ambient environment post-synthetically. While the shell thickness increases with increasing Si bisamidinate concentration, the core size decreases from 190 to 140 nm with increasing bisamidinate concentration (Figure 1J), probably resulting from more extensive oxidation with increased nitrogen content. The low index shell is thus obtained while simultaneously decreasing the core diameter to values that are favorable for visible light scattering.

Particles made with pure trisilane are consistently larger than the core–shell particles. Adding a small amount of Si bisamidinate significantly decreases the overall particle size, dropping the diameter from 370 nm for pure trisilane to below 200 nm for the 1/40 ratio (Figure S3, Supporting Information). However, as more Si bisamidinate is added, the particle size increases, with the 1/5 ratio having nearly the same diameter as particles made

from pure trisilane. We hypothesize that as the SiO_xN_y shell fills more volume than pure silicon, the total diameter increases with increasing shell thickness.

A narrow size distribution is important for a homogeneous optical response, where size dispersion was also dependent on the precursor ratio (Figure 1J). The error in size distributions in Figure 1J takes into account particles from multiple batches. Particles made from pure trisilane were highly uniform within a single batch, but the particle size from one batch to another could vary substantially. Adding Si bisamidinate led to higher batch-to-batch reproducibility, but slightly larger size dispersion within a batch. This supercritical synthesis technique produces milligrams of uniform particles in a single batch, while giving control over architectural design.

According to X-ray diffraction (XRD) patterns, selected area electron diffraction (SAED) (Figure S5, Supporting Information) and Raman scattering (Figure 1K), all the different batches have the same bond order, regardless of the relative amount of Si bisamidinate added. The XRD pattern exhibits two broad signals at 28.5° and ≈51°, which are typically associated with amorphous silicon.[24] However, Raman spectroscopy, which is more sensitive to short range order than both SAED and XRD,[21] indicates that silicon cores possess an intermediate bond order between amorphous silicon and crystalline silicon, as all batches show a relatively sharp peak at ≈500 cm^{-1}. In fact, fully amorphous silicon has a broad Raman shift at about 480 cm^{-1}, while the crystalline form has a sharp, intense Raman shift at 522 cm^{-1}.[21,25–27] Intermediate bond order implies that the particles contain high-order inclusions, consisting of linear chains of ordered tetragonal silicon (chain-like objects) or of nanocrystalline domains of about 1–2 nm, embedded in the amorphous silicon matrix.[21,26] The Raman and XRD results are not in contrast, if we consider that the crystalline domains are very small and randomly oriented, and therefore subject to Scherrer broadening.[21,24] As for the SiO_xN_y coating shell, the absence of any additional peak in the XRD patterns indicates that the shell is completely amorphous.

Fourier transformed infrared (FTIR) spectroscopy (Figure 1L) reveals the presence of Si–H and Si–OH bonds in the particles, though their relative intensity varies with changing precursor ratio. The intensity of the SiO_x bond stretching (at ≈1050 cm^{-1})[21,28] and of the O_y–SiH_x bond wagging (at ≈880 cm^{-1})[29] increases with respect to the SiH_x bond stretching (≈2100 cm^{-1})[21,28] and bending (≈660 cm^{-1})[28] for increasing molar ratios of the silicon bisamadinate complex. This trend confirms that SiO_xN_y shell thickness increases with increasing molar ratio, as observed by scanning transmission electron microscopy coupled with energy dispersive X-rays spectroscopy (STEM-EDX).

Nucleation may occur through an intermolecular reaction between trisilane and the silicon bisamidinate complex. Silicon hypervalent centers have enhanced Lewis acidity by both attachment of strong electron withdrawing groups and ring strain,[30] with reports of super Lewis acidity in such silanes.[31] The silicon bisamidinate complex contains two chlorine atoms that collectively withdraw electron density from one side of the complex and two 4-membered rings from the other side. It is thus reasonable to believe that this complex is electrophilic. On the other hand, trisilane decomposes through 1,2-H-shifts to form disilane and silylene (R_2Si:) at 250 °C.[32] Silylene is a Lewis base and a nucleophile,[33] and is thus

apt to react immediately with the electron depleted bisamidinate complex to form a new adduct, which may act as a nucleus for the growth of the silicon-based particles. Probably, the amidinate ligand, liberated at low temperature upon the reaction between the silicon bisamidinate complex and trisilane, and other nitrogen-containing degradation products, are incorporated into the architecture near the end of the reaction when the reaction temperature is highest, the trisilane concentration begins to dwindle and the reaction kinetics slow.

3. Optical Properties of Core–Shell Silicon Resonators

Dark field single particle scattering shows that the scattering properties of individual particles are affected by particle size and morphology.[34] Figure 2A–D shows a series of dark field images of four different particles resulting from different Si bisamidinate to trisilane ratios, each one representative of its batch, along with the dark field scattering spectra and the simulations performed using Mie theory (experimental details described in the Experimental Section).[35]

The scattering spectrum of a spherical core–shell particle is fully determined by the Mie theory if the following information is known: the refractive index of the particle and of its environment, the radii of the core and of the shell. The refractive index of individual particles can be retrieved through the best match of the calculated and measured scattering spectra. Knowing the outer diameter from scanning electron microscopy (SEM) measurements, we varied the shell thickness—within the experimental uncertainty given by the STEM-EDX analysis—and the refractive indexes of the core and the shell (Table S2, Supporting Information). The unknown effective refractive indexes of the core and the shell are assumed to be homogeneous. Four unknown functions of the wavelength are thus to be determined, namely, the real and imaginary parts of both the core and the shell, linked two by two by the Kramers–Kronig relation. In order to build the appropriate trial functions, we define the core as a composite material made of a ternary mixture of crystalline silicon, amorphous silicon and a low refractive index medium (equivalent to that of water) and we use the simple Maxwell–Garnett mixing rule to estimate the value of the effective indexes (see Equation (1)). The Maxwell–Garnett effective permittivity ε_{eff} of the core, made of two different inclusions of permittivity $\varepsilon_{1,2}$ and volume fraction $f_{1,2}$, in a host medium of permittivity ε_{h} reads[36]

$$\frac{\varepsilon_{\text{eff}} - \varepsilon_{\text{h}}}{\varepsilon_{\text{eff}} + 2\varepsilon_{\text{h}}} = \sum_{\text{m}=1}^{\text{M}} f_{\text{m}} \frac{\varepsilon_{\text{m}} - \varepsilon_{\text{h}}}{\varepsilon_{\text{m}} + 2\varepsilon_{\text{h}}} \quad (1)$$

The dispersion of the real and imaginary parts of the refractive indexes is obtained by the square root of the effective permittivity. The choice of amorphous and crystalline silicon comes from the Raman results, which indicate intermediate bond order. The low index medium accounts for the presence of low index inclusions, including a certain degree of hydrogenation, arising from the bottom-up synthesis method.[21,22] The fractions of amorphous silicon and low index medium control the imaginary and real parts of the effective indexes respectively, while the Maxwell–Garnett rule guarantees the Kramers–Kronig relationship. Thus, the number of free parameters reduces to two constants, namely,

the volume fractions of amorphous silicon and low index medium. The refractive index of the shell is also estimated by applying the Maxwell–Garnett rule to a two-component mixture made of low-index inclusions in silica. The resulting effective refractive index is slightly lower than the index of silica, arising from microporosity and the presence of nitrogen. Let it be clear that this model is only a convenient tool to construct a physical effective index and should not be taken as a structural model.

The scattering profile, red-shifting as particle size increases (Figure 2A–D), is well reproduced by the simulation. The dark field experimental scattering spectra are displayed (Figure 2E–H) with the computed scattering from the optimized refractive indexes (Figure 2I–J). The particle obtained with pure trisilane shows dipolar and quadrupolar resonances in the visible spectrum, with magnetic dipole resonance at about 800 nm. This indicates that the size of the core of pure trisilane particles is noticeably larger than that of the silicon cores in the core–shell particles. Moreover, even if these particles do not show a sharp core–shell boundary, the presence of a shell with a thickness of 70 nm had to be considered in order to obtain the best match between the experimental and simulated spectra. The simulations of core–shell particles show that the magnetic and electric dipole partially overlap in the visible spectrum. The broadband superposition of the magnetic and electric resonances is due to the presence of the low-index shell. The thicker the shell, the higher the ratio between the intensity of the magnetic and electric dipole resonance. Indeed, it has been predicted that a thicker shell increases the intensity of the forward scattering.[19] Bare silicon particles with the same radius and refractive index as the Si cores of the core–shell particles, present well separated dipoles in absence of a low index coating shell (Figure 2L).

In complement to single particle dark field spectroscopy, we studied the scattering from an ensemble of dispersed particles by polarization-resolved static light scattering (SLS), in order to assess the quality and homogeneity of batches made by bottom-up synthesis. The case of a colloidal suspension of isotropic scatterers has been solved by Sharma.[37] SLS analyzes the polarization of the scattered light at a scattering angle of 90°. Briefly, the magnetic dipole and the electric quadrupole scatter polarized light parallel to the scattering plane (axial scattering) while the electric dipole and the magnetic quadrupole scatter polarized light perpendicular to the scattering plane (transverse scattering),[16,38] therefore, the contribution of the magnetic dipole to the total scattering can be separated from the electric dipole based on their polarization.

Axial and transverse scattering were simulated using the scattering matrix formalism and the Mie theory[35] (Figure 3F–I). The size distribution of each batch was considered (Figure 3E), as monodispersity sharpens the scattering peaks and maximizes the scattering efficiency. The monodispersity of the sample with a 1/5 ratio is illustrated in the inset of Figure 3E, for which the particle size distribution is below 5%. As dark field data indicate that the shell of the particles synthesized with bisamidinate has a refractive index of about 1.42 ± 0.01 (Figure 2K), we chose to perform SLS measurements in chloroform, a solvent with a matching refractive index of about 1.45 at optical frequencies. The contribution of the shell to scattering hence vanishes and the scattering reduces to the contribution of bare silicon cores. The particles considered have a radius $R_c = R - t$, where R is the total particle radius and t is the average shell thickness. The index matching of the coating shell is not

as good for the pure trisilane particles. In this case we neglected the presence of the diffuse shell and considered these particles as composed of pure silicon with a very thin passivation layer.

As in the case of the single particle dark field scattering, the refractive index and absorption coefficient of the silicon cores were constructed with the Maxwell–Garnett mixing rule (details are reported in Table S3, Supporting Information). The refractive indexes and extinction coefficients obtained from SLS (Figure 3J,K) are in good agreement with the values obtained from the dark field scattering for the core–shell particles (Figure 2I,J). Let us note that the refractive indexes obtained—mostly above 3.0—albeit lower than the index of pure, compact silicon, are among the highest indexes reported in the visible spectrum. The absorption coefficient k is an intermediate value between those of amorphous and crystalline silicon. Dark field and SLS analyses both confirm these particles display high refractive index and low absorption.

In order to further compare the SLS and dark field results, the optical response of an average single particle was calculated in air using the refractive indexes and absorption coefficients retrieved from SLS (Figure S6I–L, Supporting Information) and the average particle size for the silicon cores. The coating shell was considered using the average shell thickness obtained by STEM-EDX and the refractive indexes obtained from dark field simulations. Both SLS and dark field simulations indicate that the ratio between the magnetic dipole and electric dipole intensity approaches 1 with increasing bisamidinate concentration (Figure 3L; Figure S6, Supporting Information). The average simulated spectra for the core–shell particles have much in common with the single particle simulated spectra. These converging results validate the core–shell model, giving confidence in the effective refractive index values and attesting to the uniformity of the particles within a batch.

Efficient forward light scattering requires superimposed dipoles.[16,19] As the Si bisamidinate to trisilane molar ratio used in the reaction was increased, the two dipolar maxima coalesced: the magnetic dipole blue shifts while the electric dipole position remains fixed (Figure 3M). Theoretical studies have shown that dipole coalescence may result from a refractive index contrast on the order of 2 between a homogeneous particle and the ambient medium.[16] Here we demonstrate experimentally that coating a high-index particle ($n > 3$) with a low index dielectric shell superimposes the dipoles, while keeping a high scattering efficiency, in agreement with the findings of Tsuchimoto et al.[19]

Figure 4 shows intensity maps of the electric and magnetic fields computed for the 1/5 amidinate to trisilane particle at $\lambda = 619$ nm, where electric and magnetic dipolar scattering coincide in the far field as shown in Figure 2G. In this example, the core radius is 75 nm and the shell thickness is 115 nm (Table S2, Supporting Information). The maxima of the resonant magnetic and electric fields are located in the core and in the shell respectively. The center of the core corresponds to a magnetic maximum and an electric minimum, whereas the electric maximum is located in the shell along the forward direction. Similar maps computed across the visible range show that the localization of the fields does not change much with wavelength (see Figure S7, Supporting Information). This computation shows

how, by tuning the core–shell morphology, the two dipole resonances can coexist within the particle.

The polar plots in Figure 5 illustrate the spectacular superiority of the core–shell architecture over a plain silicon sphere for the production of Huygens sources. The scattering diagrams of the non-coated silicon sphere of radius 75 nm demonstrate equal forward and backward scattering at 500 and 600 nm, where the electric and magnetic dipoles, respectively, dominate. Almost total backward scattering is observed at 550 nm, where ED and MD are opposite, and relatively weak total forward scattering is seen at 656 nm, where the electric and magnetic dipoles coincide. On the other hand, over the same range, the scattering diagrams of the core–shell particle, computed for the 1/5 amidinate to trisilane particle described in Figure 2G, exhibits intense broadband forward scattering from 500 to 750 nm with a scattering efficiency consistently above 1.3, and a maximum of 2.8 at 600 nm.

4. Conclusions

The potency of the bottom-up chemical approach is in its versatility. This first large-scale bottom-up synthesis of core–shell silicon-based nanospheres surpasses materials produced by top-down methods. The size and the shell thickness are controlled by changing the relative concentration of two molecular precursors. The richness of the core–shell architecture allows a fine tuning of Mie resonances in the visible spectrum. SLS and single particle scattering show that the two resonances tend to overlap as the shell thickness increases, fulfilling the conditions of a Huygens source. For a shell thickness similar to the core diameter, not only do the two resonances occur throughout the same broad wavelength range, but the magnetic and electric dipolar modes have nearly the same amplitude. Over a broad range of visible frequencies, the core–shell particle outperforms the pure silicon particle both in intensity and directionality of forward scattering. These properties are crucial for the development of metasurfaces composed of broadband Huygens sources. Moreover, regarding the strength of the dipolar magnetic Mie resonances, these particles are suitable for the fabrication of a bulk artificial material with effective magnetic permeability significantly different from 1 in the visible.

5. Experimental Section

Materials:

Trisilane was purchased from Voltaix, and stored in a glovebox (oxygen level < 0.1 ppm). *N,N′*-diisopropylcarbodiimide (99%), silicon tetrachloride (99%), butyl-lithium (2.5 M in hexane), n-hexane (anhydrous 95%), chloroform, and absolute ethanol were purchased from Sigma-Aldrich and used without further purification. Toluene and THF were dried using an Innovative Technology solvents purification system, then oxygen was removed by three freeze–pump–thaw cycles. The purified solvents were stored over 3 Å molecular sieves in an argon filled glovebox.

Synthesis of bis(N,N′-diisopropylbuyl)Dichlorosilane:

The synthesis of bis(*N,N′*-diisopropylbutyl)dichlorosilane, $[(iPr\text{-}N)_2C(C_4H_9)]_2SiCl_2$ **(2)**, was carried out under inert atmosphere, using Schlenk techniques to protect reactants and

products from moisture and oxygen, by modifying previously published protocols.[39,40] The bis(*N,N′*-diisopropylbuyl) dichlorosilane, or silicon bisamidinate for simplicity, has been prepared by a two-step synthesis (see reaction scheme in Figure S1, Supporting Information). Butyl-lithium (13 mL, 0.032 mol) was added to a solution of *N,N′*-diisopropylcarbodiimide (5 mL, 0.032 mol) in THF (80 mL) at −30 °C under magnetic agitation. This reaction yields the compound lithium (*N,N′*-diisopropylbutylamidinate), $[(iPrN)_2C(CH_3)]Li{\cdot}THF$ **(1)**.

^{1}H NMR **(1)** (400 MHz, C_6D_6, 25 °C): δ 0.9489 (t, 3H, $^3J_{HH}$ 7.20 Hz, $CH_3(CH_2)_4C$), δ 1.3271 (d, 12H, $^3J_{HH}$ 6.64 Hz, ^{i}Pr-CH_3), δ 1.4047 (m, 4H THF, CH_2), δ 1.40 (m, 2H $CH_3CH_2CH_2CH_2C$), δ 1.6152 (m, 2H, $CH_3CH_2CH_2CH_2C$), δ 2.3910 (m, 2H, $CH_3(CH_2)_2CH_2C$), δ 3.5795 (m, 4H THF, CH_2O), δ 3.7236 (m, 2H, $(CH_3)_2CH$).

Typically, the product (**1**) was not isolated and purified. The reaction was stirred overnight at room temperature to ensure complete reaction. Then, $SiCl_4$ (1.86 mL, 0.016 mol) was added at −78 °C. The solution was stirred at room temperature for 18 h. The solvent was evaporated and substituted with toluene (60 mL). The solution was filtered, and silicon bisamidinate was crystallized from the filtrate by slow evaporation of the toluene.

Silicon bisamidinate was stored at −15 °C, under an argon atmosphere, to avoid premature degradation, as it is extremely sensitive to moisture and thermally labile.

^{1}H NMR **(2)** (400 MHz, C_6D_6, 25°C): δ 0.7662 (t, 6H, $^3J_{HH}$ 7.4424 Hz, Bu-CH_3), δ 1.0995 (d, 6H, $^3J_{HH}$ 6.5221 Hz, ^{i}Pr-CH_3), δ 1.133(m, 4H, $^3J_{HH}$, CH_3CH_2 $(CH_2)_2C$), δ 1.3851 (d, 6H, $^3J_{HH}$ 6.6822, ^{i}Pr-CH_3), δ 1.38 (m, 4H, $CH_3CH_2CH_2CH_2C$), δ 1.5964 (d, 6H, $^3J_{HH}$ 7.0023 Hz, ^{i}Pr-CH_3), δ 1.6313 (d, 6H, $^3J_{HH}$ 6.8822 Hz, ^{i}Pr-CH_3), δ 2.0084 (m, 4H, $CH_3(CH_2)_2CH_2C$), δ 3.5014 (sept. 2H, $^3J_{HH}$ 6.7622 Hz, ^{i}Pr-CH), δ 4.1844 (sept. 2H, $^3J_{HH}$ 8.9229 Hz, ^{i}Pr-CH).

Supercritical Synthesis of the Silicon Core–Shell Particles:

The supercritical synthesis was carried out in a 10 mL titanium (alloy grade 2) batch reactor, purchased from High Pressure equipment (HiP) (part number 210617). This kind of reactor can withstand a maximum pressure and temperature of 345 bar (5000 psi) and 600 °C. The synthesis protocol was similar to what has been reported previously about the supercritical synthesis of silicon nanoparticles.[21–23] The reactor was loaded and sealed in a nitrogen filled glovebox (O_2 < 0.1 ppm) with n-hexane (5.6 mL), trisilane (5 μL, 40.2 μmol), and a variable amount of silicon bisamidinate (caution: trisilane is pyrophoric and must be handled with extreme care under inert atmosphere). The molar ratios, concentration, and number of moles of silicon bisamidinate and trisilane used in the reactions are summarized in Table S1 of the Supporting Information. The reactor was placed in a ceramic heating block that was preheated to 510 °C, using a dummy reactor. Supercritical synthesis was carried out at 460 °C and 300 bar, for a duration of 10 min. After 10 min, the reactor was removed from the heating block and placed in an ice bath to quench the reaction. Once the reactor cooled to room temperature, it was opened and the products collected under air. The resulting product was centrifuged at 8000 rpm for 5 min, to precipitate the nanoparticles and discard the solvent. This cycle was repeated three more times, using chloroform to wash the products.

The nanoparticles were stored in a nitrogen-filled glovebox as a dry powder to avoid any further oxidation. The supercritical reaction yields about 2.0–2.7 mg of dry particles, which correspond to a mass yield of about 50% (only in the case of the 1/5 silicon bisamidinate to trisilane ratio, the mass yield was about 30%).

Each experiment was repeated at least twice (for 1/40 and 1/5 ratio) or three times (for pure trisilane and 1/20 ratio) to ensure reproducibility in terms of particles size and dispersion.

SEM Characterization:

SEM images were acquired using a Zeiss Supra 40 VP SEM, with an accelerating voltage of 5 keV. The samples were prepared by drop-casting a colloidal suspension of Si nanoparticles in chloroform onto the polished face of p-doped silicon wafer.

STEM-EDX Characterization:

SAED, bright and dark field TEM imaging, and elemental mapping of the Si particles were carried out using a Talos F200S G2 TEM (ThermoFisher, Eindhoven), using an accelerating voltage of 200 kV. STEM-EDX analysis and TEM imaging were performed on cross-sectioned particles. The samples were prepared by including free-standing particles in the form of a dry powder into an epoxy resin (Epon 812; Delta Microscopies, Toulouse, France) using beam capsule conical tips. The polymerization of the resin was carried out at 60 °C over a period of 24–48 h.

The resin containing the particles was then sectioned using a diamond knife (Diatome, Biel-Bienne, Switzerland) on an ultramicrotome (EM UCT, Leica Microsystems, Vienna, Austria). Ultrathin sections (70 nm) were placed on copper grids with a carbon membrane for observation.

FTIR Spectroscopy:

FTIR spectra of the particles were collected using a Bruker Vertex 70 FTIR. A colloidal solution of particles in chloroform was drop-cast onto a double polished silicon wafer support. The sample was then placed in the optical path of the beam. During the measurement, a stream of nitrogen was flushed through the IR chamber in order to evacuate CO_2 and water. The infrared spectra have been normalized with respect the Si–H_x stretching mode (≈2100 cm^{-1}).

Raman Scattering:

Raman spectra were collected with an Xplora spectrometer by Horiba, equipped with a confocal microscope. Samples were prepared by drop casting Si nanoparticles suspended in chloroform onto a glass microscope slide. An objective lens with a magnification of 50× was used to observe the sample and choose the measurement area. A 100× objective lens was employed to focus the laser beam on the selected spot. The spectra were run using a 532 nm excitation wavelength, using a filter to reduce the laser power to 50% of the total power. A 1800T grating was used to separate the scattered light into its components. Baseline subtraction was performed on each spectrum, using a linear baseline. Five measurements

in five different zones were collected for each sample, to assess the reproducibility of the measurement and the uniformity of the sample.

X-Ray Diffraction:

Powder X-ray diffraction spectra were performed using a Rigaku Spider diffractometer operated at 40 kW and 40 mA, with a Cu anode $\left(\lambda = 1.54\ \text{Å}\right)$.

Nuclear Magnetic Resonance:

Proton nuclear magnetic resonance spectra (^{1}H NMR) of the silicon bisamidinate were acquired using a Bruker Advance III-HD 400 MHz SB spectrometer (Wissembourg, France) equipped with a 5 mm broadband SmartProbe at 25 °C in C_6D_6. ^{1}H NMR spectra were acquired at 400.13 MHz using a single pulse sequence ($\pi/2$ pulse width of 10 μs, recycling delay of 2 s, acquisition time of 1.6 s, spectral window of 25 ppm and 24 scans).

Dark Field Single Particle Scattering:

Dark field scattering spectra of particles were measured using an inverted microscope (Ti-E, by Nikon) operating in transmission mode, equipped with a halogen light source (12 V, 100 W), a CCD camera and spectrograph (by Andor), an oil objective (100×), and a dark field condenser.[34]

Samples were drop-cast from dilute suspensions of particles in ethanol onto a microscope glass slide. The slide was placed between the dark field condenser and the oil objective. Scattered light was collected through the objective with the spectrometer, while dark field images of the particles were collected using the CCD camera. The aperture number of the oil objective was 0.5, while the aperture number of the dark field condenser was 1.43–1.20.

DF measurements were carried out on ten particles in each batch to check the uniformity of the observations. An excellent reproducibility was obtained within each batch.

Static Light Scattering:

Polarization resolved static light scattering was carried out using a custom-built set-up. The scattering matrix formalism linking the incident field E_i to the scattered field E_{scat} (Equation (2)) was used.[35] The plane was defined by the directions of the incident and scattered fields, forming the scattering plane. The subscripts // and ⊥ signify the field components parallel (axial) and perpendicular (transverse) to the scattering plane respectively. For isotropic scatterers, such as spheres, the off-diagonal elements of the scattering matrix are zero

$$\begin{pmatrix} E_{\text{scat.}//} \\ E_{\text{scat.}\perp} \end{pmatrix} = \frac{e^{iqr}}{-iqr} \begin{pmatrix} S_2(\theta) & 0 \\ 0 & S_1(\theta) \end{pmatrix} \begin{pmatrix} E_i \cos\varphi \\ E_i \sin\varphi \end{pmatrix} \quad (2)$$

Theta (θ) is the scattering angle and phi (φ) is the angle between the scattering plane and the direction of the polarization of incident light (see Figure S2, Supporting Information). At a scattering angle θ of 90°, the odd and even scattering modes are separate: the S_1 element

cumulates the scattering contribution of the electric dipole, magnetic quadrupole, electric octupole, etc. while the S_2 element contains the contribution of the magnetic dipole, electric quadrupole, magnetic octupole, etc.[35,37,38,41]

The experimental geometry is shown in Figure S2 of the Supporting Information. The light source is a super continuum laser (SuperK EXB-6 with SuperKSplit filter from NKT Photonics) emitting from 440 to 900 nm. The incident beam was linearly polarized by a Glan–Taylor polarizer (Thorlabs GL5-A) and the polarization angle phi was controlled by the rotation of a tandem Fresnel rhombohedrum acting as an achromatic half-wave retarder (Thorlabs FR600HM).

The sample consisted of a colloidal suspension of silicon particles in chloroform placed in a fused silica cuvette. The scattered light was collected at $\theta = 90^{\circ}$ with respect to the direction of incident light, using a Minispectrometer (Hamamatsu C10083CA) fed with a collimated optical fiber. A second Glan–Taylor polarizer (Thorlabs GL10-A), placed between the sample and the detector, analyzed the scattered light with parallel (axial) or perpendicular (transverse) polarization. Scattering spectra were collected over a 360° rotation of the φ angle at intervals of 10°. The intensities measured along the transverse and axial directions are as follows

$$I_{\perp s} = I_0(\lambda) \cdot \left(N_{\text{scat}}/q^2\right) \cdot \left|S_1(\theta = 90^{\circ})\right|^2 \cdot \delta\Omega \cdot T(\lambda) \cdot g(\lambda, \delta\Omega) \cdot \sin^2\varphi = B_{\perp}(\lambda) \cdot \sin^2\varphi \quad (3)$$

$$I_{//s} = I_0(\lambda) \cdot \left(N_{\text{scat}}/q^2\right) \cdot \left|S_2(\theta = 90^{\circ})\right|^2 \cdot \delta\Omega \cdot T(\lambda) \cdot g(\lambda, \delta\Omega) \cdot \cos^2\varphi = B_{//}(\lambda) \cdot \cos^2\varphi \quad (4)$$

where $I_0(\lambda)$ is the spectral irradiance of the incident beam, N_{scat} represents the number of particles in the scattering volume, q is the wave number $(2\pi/\lambda)$. The solid angle $\delta\Omega$ represents the detection window, $T(\lambda)$ is the transmittance of the suspension, and $g(\lambda, \delta\Omega)$ is an unknown function of the instrument, dependent on the spectral power of the source, the sensitivity of the detector, and the transmittance and reflectance of all the optical elements.

The experimental axial and transverse scattering have been fitted for each wavelength with functions of the type $A_{\parallel} + B_{\parallel}\sin^2(\varphi)$ and $A_{\perp} + B_{\perp}\cos^2(\varphi)$ respectively. The background signals $A_{\parallel}$ and $A_{\perp}$ measure a residual anisotropy of the scatterers[42] which were below 10% in most of the tested samples.

The differential scattering cross-section of the transverse even modes (i.e., mostly ED and MQ in silicon particles) and axial odd modes (i.e., mostly MD and EQ) were obtained by normalizing the parameters $B_{\perp}$ and $B_{//}$ by the parameter B_{ref} of a known reference sample. A colloidal suspension of silica (SiO_2) beads with diameter of 120 nm was used. In this size range, silica does not exhibit any Mie resonance, and, most importantly, its scattering cross-section was simply calculated from the Mie theory[35,38,43]

$$\sigma_{\perp}^{\theta=90^{\circ},\varphi=0^{\circ}} = \left|S_1(\theta=90^{\circ})\right|^2/q^2 = (N_{\text{ref}}/N_{\text{scat}})\cdot(B_{\perp}/B_{\text{ref}})\cdot(T_{\text{ref}}(\lambda)/T_{\perp}(\lambda))\cdot\sigma_{\text{ref}}^{\theta=\varphi=90^{\circ}} \quad (5)$$

$$\sigma_{//}^{\theta=\varphi=90^{\circ}} = \left|S_2(\theta=90^{\circ})\right|^2/q^2 = (N_{\text{ref}}/N_{\text{scat}})\cdot(B_{//}/B_{\text{ref}})\cdot(T_{\text{ref}}(\lambda)/T_{//}(\lambda))\cdot\sigma_{\text{ref}}^{\theta=\varphi=90^{\circ}} \quad (6)$$

where N_{ref} and N_{scat} are the number of particles in the scattering volume for the SiO_2 reference and the silicon sample respectively. The concentration ratio $N_{\text{ref}}/N_{\text{scat}}$, which could not be determined with sufficient accuracy, was accounted for with an unknown scaling constant K. Since the colloidal suspensions containing sample and reference must be highly diluted to prevent multiple scattering, the transmittances $T(\lambda)$ of the sample and $T_{\text{ref}}(\lambda)$ of the reference, were simply the transmittance of the pure solvent so that the transmittance ratio appearing in Equations (5) and (6) equaled 1.

Maxwell–Garnett Model:

The Maxwell–Garnett model[36] (Equation (1)) was used to build the effective permeability of the silicon core and of the shell. The complex effective refractive index $N = n + ik$, is the square root of the effective permittivity. Effective permittivity was constructed by considering the particles to be composed of a mixture of crystalline silicon, amorphous silicon, and low index inclusions (refractive index equivalent to water). The index dispersion for amorphous and crystalline silicon were obtained from the data collected by Pierce and Spicer[44] and Aspnes and Studna[45] respectively, available on an online database.[46] To simulate the presence of low index impurities, included within the particles, a refractive index equal to water was used.[47] This model allows the volume fraction, f_m, of c-Si, a-Si, and low index impurities to be adjusted in order to obtain the best agreement between simulations and experiments,[36] while respecting the Kramers–Kronig conditions.

Dark Field Scattering Simulation:

The scattering spectra of the silicon particles were computed from the Mie theory which provides exact analytical expressions of the scattering efficiency by both homogeneous spheres and spherical core–shell structures.[35] The control parameters were the size and refractive index of the core and the shell.

The single particle dark field scattering simulations were carried out considering both the angle of incident light (55°–80°) and the cone of acceptance of scattered light, spanning from 0° to 30°. The angle of incident light, from 55° to 80°, was determined from the numerical aperture of the dark field condenser, while the angle of collection was determined from the numerical aperture of the oil immersion objective. The scattering spectra of single particles with total radius R, core radius R_c, and shell thickness $t = R - R_c$, were simulated. The variable m_2 represent the contrast between the coating shell index and the medium, and the variable m_1 is the contrast between the Si index core and the medium. In this case, the surrounding medium was defined as air.

The particle radius, R, is the only parameter known with accuracy from SEM measurements, and it is not varied during the simulation (see Figure 2A–D). The shell thickness, t (or equivalently the core size, R_c) is optimized around the average values obtained from TEM-EDX (see Tables S2 and S3 of the Supporting Information for comparison between the optimized and average values).

The Si core refractive index and absorption coefficient, as well as the shell refractive index, were varied according to the Maxwell–Garnett model, by adjusting the volume fraction of crystalline and amorphous silicon, and of low index impurities (see subsection above). By optimizing the refractive index and absorption coefficient, as well as t, the best accord between simulated and experimental data could be obtained. The wavelength dispersions of the refractive index and absorption coefficient are presented in Figure 2I–J, along with the wavelength dispersion of crystalline and amorphous silicon. The optimized t and R_c are presented in Table S2 (see Tables S2 and S3 of the Supporting Information for comparison between the optimized and average values). The simulations of dark field scattering obtained by optimizing n, k, and t are presented in Figure S6A–D of the Supporting Information along with the experimental dark field scattering. The optimized parameters were used for computing the total scattering efficiency, magnetic and electric dipoles and quadrupoles scattering efficiency of the single particle in air (Figure S6, Supporting Information). The field maps shown in Figure 4 represent the exact Mie solution for a coated sphere computed as an expansion in vector spherical harmonics with the appropriate set of scattering coefficients.[35]

Static Light Scattering Simulation:

In contrast with DF, static light scattering collects the scattering of an ensemble of particles suspended in the scattering volume. The statistic size distribution must therefore be taken into account. In the case of highly dilute suspension, multipole scattering, and EM coupling between particles was negligible, so that the scattering of all particles added up, weighted by their probability of occurrence. The probability $\mathrm{P}(R_i)$ of particle occurrence with a certain radius, R_i, was estimated from the histograms reported in Figure 3E. The histograms were built by measuring the size of 200 particles for each batch and distributing the sizes in bins of width 8 nm.

The scattering cross sections for the transverse (S_1) and axial (S_2) scattering, $\sigma_\perp(R_i)$, and $\sigma_\parallel(R_i)$, are then given by

$$\sigma \perp = \frac{1}{q^2}\left|S_1(\theta = \pi/2)\right|^2 \tag{7}$$

$$\sigma_\parallel = \frac{1}{q^2}\left|S_2(\theta = \pi/2)\right|^2 \tag{8}$$

$$\sigma_\perp^{\text{total}} = \sum_{R_i} \sigma_\perp(R_i)\mathrm{P}(R_i) \tag{9}$$

$$\sigma_{\parallel}^{\text{total}} = \sum_{R_i} \sigma_{\parallel}(R_i)\mathrm{P}(R_i) \tag{10}$$

As mentioned in the main text, the presence of the coating shell was neglected, since it has a refractive index very close to the refractive index of chloroform (Figure 2K).[46,48] Therefore, the size distribution of the silicon cores was considered for the computation of the axial and transverse scattering cross-section (Equations (9) and (10)).[35] The silicon core size distribution was calculated by subtracting the average shell thickness, t, calculated thanks to the STEM-EDX characterization (see Table S3, Supporting Information) from each value of the total radius R_i (reported in the histograms in Figure 3). By doing so, the size histograms were shifted to smaller values by a factor $2t$. The average shell thickness and size distribution were experimentally known, and were considered as constant parameters during the simulations. The dispersion of the refractive index and absorption coefficient of the silicon cores were optimized for each batch, in order to obtain the best simulations of the experimental spectra, using the Maxwell–Garnett mixing rule (Equation (1)).

These values were then used to calculate the scattering efficiency of an isolated core-shell particle in vacuum, having total radius, R, and shell thickness, t equal to the average values for each batch (Figure S6I–L and Table S3, Supporting Information). The refractive index used for the coating shell was obtained from DF simulations (Figure 2K).

Supplementary Material

Refer to Web version on PubMed Central for supplementary material.

Acknowledgements

Benoît Cormary helped with the bisamadinate precursor synthesis. MLDM and GLD were supported by the LabEx AMADEus (ANR-10-LABX-42) in the framework of IdEx Bordeaux (ANR-10-IDEX-03-02), i.e., the Investissements d'Avenir program of the French government managed by the Agence Nationale de la Recherche. B.A.K. and T.J. acknowledge financial support of this work from the Robert A. Welch Foundation (F-1464) and the National Science Foundation through the Center for Dynamics and Control of Materials, an NSF MRSEC under Cooperative Agreement No. DMR-1720595. J.F. and Y.Z. acknowledge the financial support of the National Science Foundation (NSF-ECCS-2001650), and the National Institute of General Medical Sciences of the National Institutes of Health (DP2GM128446). STEM-EDX imaging was performed on the Bordeaux Imaging Center, member of the FranceBioImaging national infrastructure (ANR-10-INBS-04).

Data Availability Statement

Data sharing is not applicable to this article as no new data were created or analyzed in this study.

References

[1]. Landau LD, Lifshitz EM, Electrodynamics of Continuous Media, Oxford University Press, Oxford 1960.

[2]. Shalaev VM, Nat. Photonics 2007, 1, 41.

[3]. Cai W, Chettiar UK, Kildishev AV, Shalaev VM, Nat. Photonics 2007, 1, 224.

[4]. Schurig D, Mock JJ, Justice BJ, Cummer SA, Pendry JB, Starr AF, Smith DR, Science 2006, 314, 977. [PubMed: 17053110]

[5]. Shelby RA, Science 2001, 292, 77. [PubMed: 11292865]

[6]. Moitra P, Slovick BA, li W, Kravchencko II, Briggs DP, Krishnamurthy S, Valentine J, ACS Photonics 2015, 2, 692.

[7]. Dezert R, Richetti P, Baron A, J. Phys. Conf. Ser. 2018, 1092, 012022.

[8]. Staude I, Miroshnichenko AE, Decker M, Fofang NT, Liu S, Gonzales E, Dominguez J, Luk TS, Neshev DN, Brener I, Kivshar Y, ACS Nano 2013, 7, 7824. [PubMed: 23952969]

[9]. Gomez-Graña S, Beulze A. L. e, Treguer-Delapierre M, Mornet S, Dugue E, Grana E, Cloutet E, Hadziioannou G, Leng J, Salmon J-B, G. Kravets V, Grigorenko AN, Peyyety NA, Ponsinet V, Richetti P, Baron A, Torrent, Barois P, Mater. Horiz. 2016, 3, 596.

[10]. Jahani S, Jacob Z, Nat. Nanotechnol. 2016, 11, 23. [PubMed: 26740041]

[11]. Wang M, Krasnok A, Lepeshov S, Hu G, Jiang T, Fang J, Korgel BA, Alù A, Zheng Y, Nat. Commun. 2020, 11, 5055. [PubMed: 33028825]

[12]. Sugimoto H, Okazaki T, Fujii M, Adv. Opt. Mater. 2020, 8, 2000033.

[13]. Hinamoto T, Hotta S, Sugimoto H, Fujii M, Nano Lett. 2020, 20, 7737. [PubMed: 32986436]

[14]. De Marco ML, Semlali S, Korgel BA, Barois P, Drisko GL, Aymonier C, Angew. Chem., Int. Ed. 2018, 57, 4478.

[15]. Decker M, Staude I, Falkner M, Dominguez J, Neshev DN, Brener I, Pertsch T, Kivshar YS, Adv. Opt. Mater. 2015, 3, 813.

[16]. Dezert R, Richetti P, Baron A, Phys. Rev. B 2017, 96, 180201.

[17]. Elancheliyan R, Dezert R, Castano S, Bentaleb A, Nativ-Roth E, Regev O, Barois P, Baron A, Mondain-Monval O, Ponsinet V, Nanoscale 2020, 12, 24177. [PubMed: 33283823]

[18]. Liu W, Miroshnichenko AE, Neshev DN, Kivshar YS, ACS Nano 2012, 6, 5489. [PubMed: 22545872]

[19]. Tsuchimoto Y, Yano T, Hayashi T, Hara M, Opt. Express 2016, 24, 14451. [PubMed: 27410598]

[20]. Naraghi RR, Sukhov S, Dogariu A, Opt. Lett. 2015, 40, 585. [PubMed: 25680156]

[21]. Harris JT, Hueso JL, Korgel BA, Chem. Mater. 2010, 22, 6378.

[22]. Shi L, Harris JT, Fenollosa R, Rodriguez I, Lu X, Korgel BA, Meseguer F, Nat. Commun. 2013, 4, 1904. [PubMed: 23695698]

[23]. Pell LE, Schricker AD, Mikulec FV, Korgel BA, Langmuir 2004, 20, 6546. [PubMed: 15274552]

[24]. Mahan AH, Yang J, Guha S, Williamson DL, Phys. Rev. B 2000, 61, 1677.

[25]. Hong W-E, Ro J-S, J. Appl. Phys. 2013, 114, 073511.

[26]. Tsu DV, Chao BS, Jones SJ, Sol. Energy Mater. Sol. Cells 2003, 78, 115.

[27]. Richter H, Wang ZP, Ley L, Solid State Commun. 1981, 39, 625.

[28]. Angi A, Loch M, Sinelnikov R, Veinot JGC, Becherer M, Lugli P, Rieger B, Nanoscale 2018, 10, 10337. [PubMed: 29683161]

[29]. Mawhinney DB, Glass JA, Yates JT, J. Phys. Chem. B 1997, 101, 1202.

[30]. Hartmann D, Schädler M, Greb L, Chem. Sci. 2019, 10, 7379. [PubMed: 31489160]

[31]. Liberman-Martin AL, Bergman RG, Tilley TD, J. Am. Chem. Soc. 2015, 137, 5328. [PubMed: 25879515]

[32]. Vanderwielen AJ, Ring MA, O'Neal HE, J. Am. Chem. Soc. 1975, 97, 993.

[33]. Tacke R, Ribbeck T, Dalton Trans. 2017, 46, 13628. [PubMed: 28945254]

[34]. Wang M, Wu Z, Krasnok A, Zhang T, Liu M, Liu H, Scarabelli L, Fang J, Liz-Marzán LM, Terrones M, Alù A, Zheng Y, Small 2019, 15, 1900982.

[35]. Bohren CF, Huffmann DR, Absorption and Scattering of Light from Small Particles, John Wiley and Sons, New York 1983.

[36]. Sihvola A, Subsurf. Sens. Technol. Appl. 2000, 1, 393.

[37]. Sharma NL, Phys. Rev. Lett. 2007, 98, 217402. [PubMed: 17677805]

[38]. Ponsinet V, Barois P, Gali SM, Richetti P, Salmon JB, Vallecchi A, Albani M, Beulze A. L. e, Gomez-Grana S, Duguet E, Mornet S, Treguer-Delapierre M, Phys. Rev. B 2015, 92, 220414.

[39]. Hao S, Gambarotta S, Bensimon C, Edema JJH, Inorg. Chim. Acta 1993, 213, 65.

[40]. Karsch HH, Schlüter PA, Reisky M, Eur. J. Inorg. Chem. 1998, 4, 433.

[41]. Dezert R, Richetti P, Baron A, Opt. Express 2019, 27, 26317. [PubMed: 31674516]

[42]. Gomez-Grana S, Treguer-Delapierre M, Duguet E, Salmon JB, Leng J, Kravets V, Grigorenko AN, Peyyety A, Ponsinet V, Richetti P, Baron A, Torrent-Marti D, Barois P, 2016 10th Int. Congress on Advanced Electromagnetic Materials in Microwaves and Optics (METAMATERIALS), IEEE, Creete, Greece 2016.

[43]. Many V, Dézert R, Duguet E, Baron A, Jangid V, Ponsinet V, Ravaine S, Richetti P, Barois P, Tréguer-Delapierre M, Nanophotonics 2018, 8, 549.

[44]. Pierce DT, Spicer WE, Phys. Rev. B 1972, 5, 3017.

[45]. Aspnes DE, Studna AA, Phys. Rev. B 1983, 27, 985.

[46]. Polyanskiy M, Refractive Index.INFO, Refractive index database [online], https://refractiveindex.info (accessed: July 2020).

[47]. Daimon M, Masamura A, Appl. Opt. 2007, 46, 3811. [PubMed: 17538678]

[48]. Samoc A, J. Appl. Phys. 2003, 94, 6167.

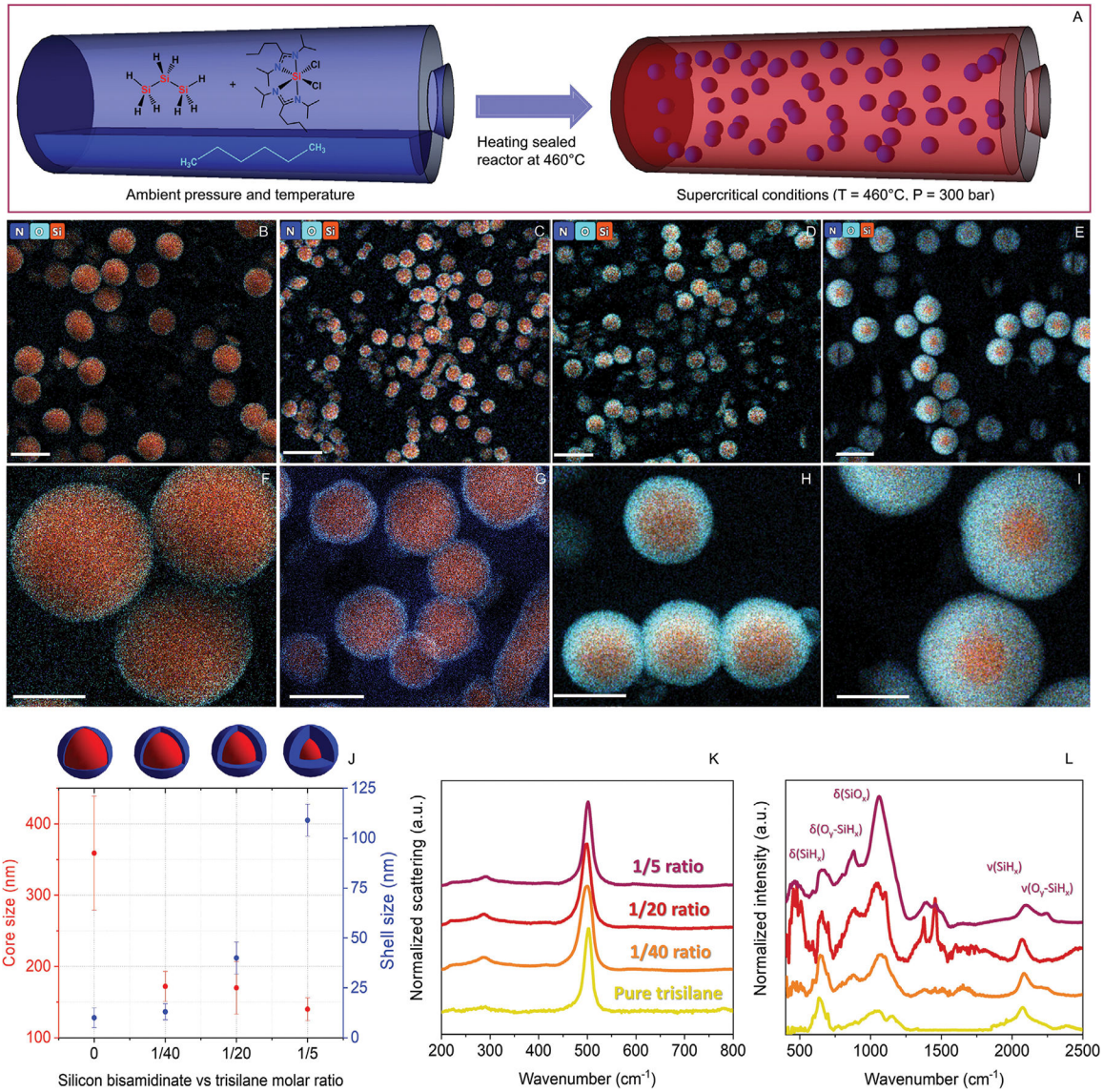

Figure 1.

Synthetic route toward optically resonant core–shell particles. A) Scheme representing the supercritical synthesis of core–shell silicon particles in a batch reactor heated to 460 °C. STEM-EDX mapping of the cross section of silicon particles realized with B,F) pure trisilane, C,G) 1/40, with D,H) 1/20, and E,I) 1/5 Si bisamidinate to trisilane molar ratio, respectively. The size of the scale bars represents 500 nm for the images (B)–(E) and 200 nm for the images (F)–(I). J) The core size and shell thickness of the particles depend on the molar ratio between the two precursors. K) Raman and L) infrared spectra of the different batches of particles, where δ represents the bending modes and ν the stretching modes.

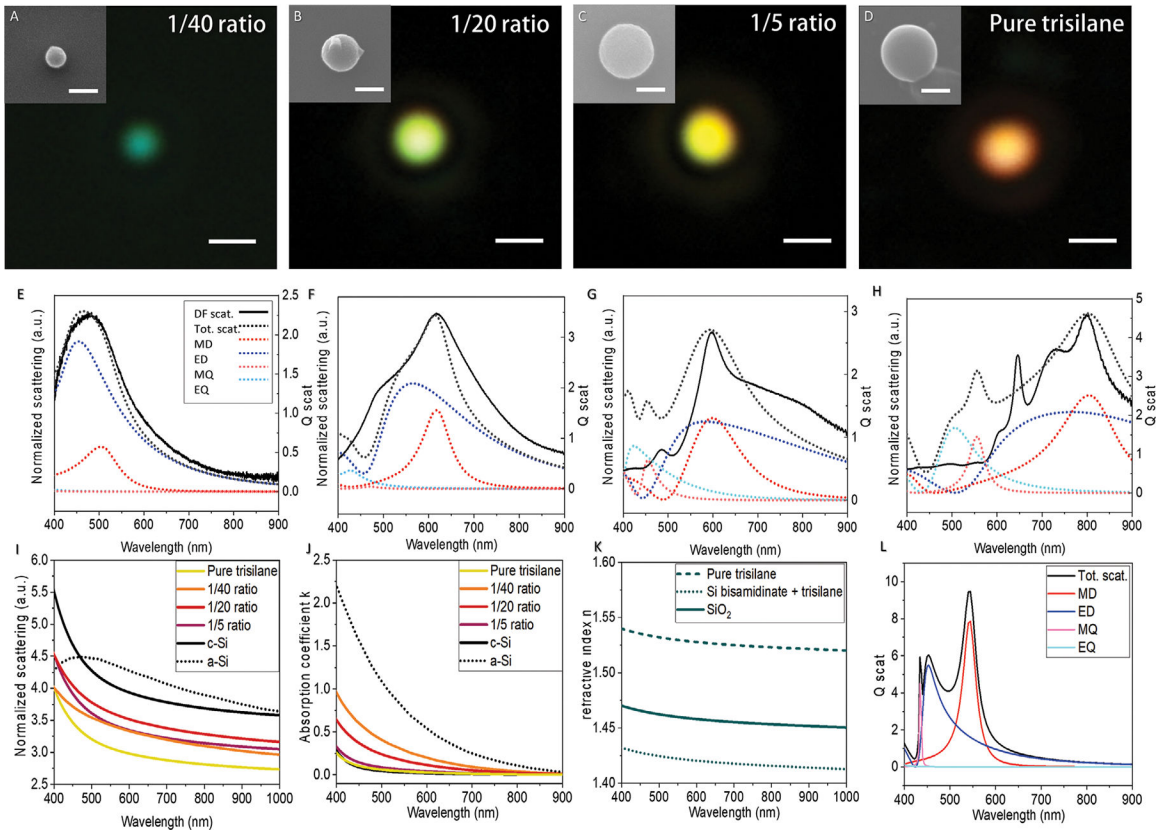

Figure 2.

Light scattering properties of single particles. Dark field images of one particle representative of each batch: A) 1/40 ratio (⌀ = 150 nm), B) 1/20 ratio (⌀ = 262 nm), C) 1/5 ratio (⌀ = 380 nm), and D) pure trisilane (⌀ = 392 nm). The size of the scale bars represents 1 μm. The insets are SEM images of the measured particle, where the size of the scale bars represents 200 nm. Experimental (solid black line) and simulated (dotted black line) total scattering and dipolar and quadrupolar scattering (dotted colored lines), for particles produced with a E) 1/40, F) 1/20, and G) 1/5 ratio, and H) with pure trisilane. I) Refractive indexes and J) absorption coefficients of the silicon cores and K) refractive index of the shell. L) Simulation of the scattering cross section of the bare Si core of the particle represented in (C) and (D) 1/5 ratio.

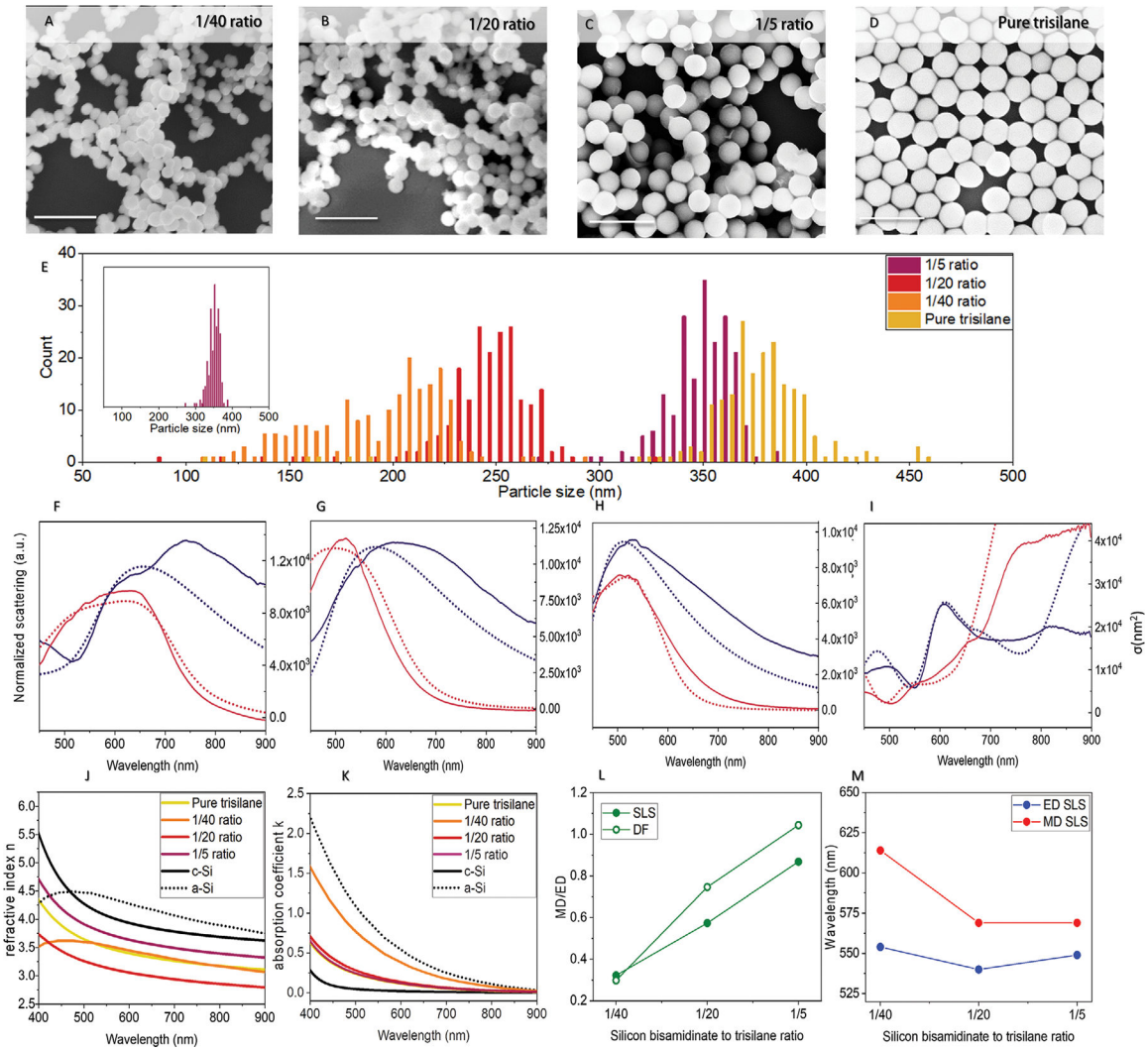

Figure 3.

Optical properties of batches of silicon particles. SEM pictures of batches of particles realized with different molar ratios: A) 1/40, B) 1/20, and C) 1/5, and D) with pure trisilane. The size of the scale bars represents 1 μm. E) Histograms showing the diameter dispersion of different batches of particles of (A)–(D), the inset shows the size distribution of the 1/5 sample. Experimental (solid lines) and simulated (dotted lines) axial (red) and transverse (blue) scattering of colloidal suspensions of particles produced with F) 1/40, G) 1/20, and H) 1/5 ratios, and I) pure trisilane. J) Refractive index and K) absorption coefficient obtained from the SLS simulations. L) Comparison of the MD/ED ratio between the dark field and the SLS data as the molar ratio increases and (M) the position of the maxima of the ED and MD resonances as a function of the Si bisamidinate relative concentration. The trends shown in (L) and (M) are extracted from the simulations in Figure 2E–H and Figure S5I–L (Supporting Information).

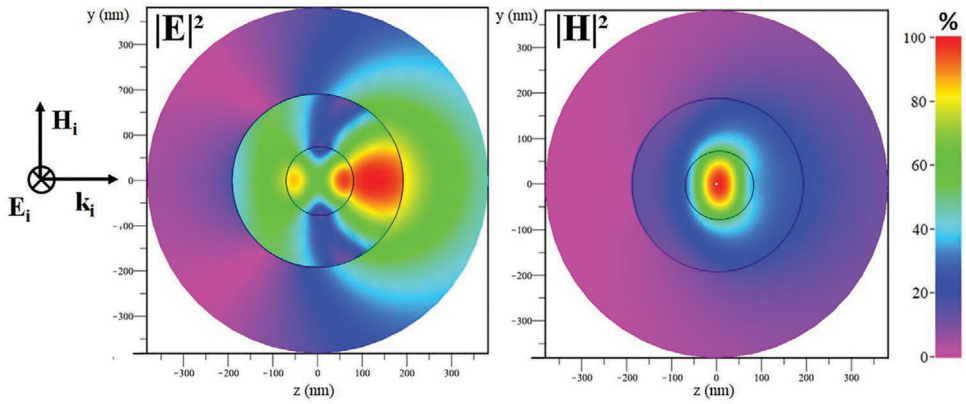

Figure 4.

Electric field (left) and magnetic field (right) intensity maps computed for the 1/5 amidinate to trisilane particle described in Figure 2G at = 619 nm, where the electric and magnetic dipolar far-field scattering coincide. The polarization is set perpendicular to the shown cutaway. The inner and outer black circles represent the core–shell and shell-free space interfaces respectively. The color scale maps the intensities as a percentage of the maximum in each case.

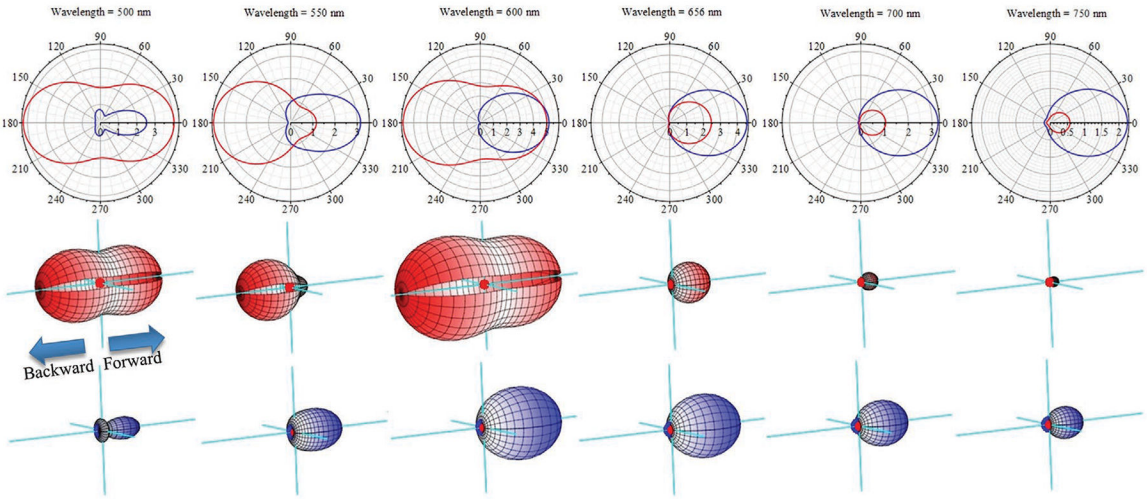

Figure 5.

Angular dependence of the scattering cross section for a core–shell and a bare silicon particle. Top row: polar plots of the differential scattering efficiency computed for the core–shell particle shown in Figure 2G (blue lines) and a reference crystalline silicon sphere of radius 75 nm (red lines) at $\lambda = 500$ nm, 550 nm, 600 nm, 656 nm, 700 nm, and 750 nm from left to right. Radial units are steradian^{-1}. Center and bottom rows: 3D scattering diagrams of the core–shell particle (blue) and the silicon reference (red), all shown at the same scale. Unpolarized incident light comes from the left in all diagrams.